Inner and Outer Surface Areas, Electrochemical Porosity, and Morphology Factor of Mixed Oxide-Covered Mesh Electrodes with a Nominal Composition of MOME-Sn$_{0.5}$Ir$_x$Ru$_{(0.5-x)}$O$_2$

José J.S. Teles, Emanuel R. Faria, Débora V. Franco, Leonardo M. Da Silva[*]

Departamento de Química, Universidade Federal dos Vales do Jequitinhonha e Mucuri, Rodovia MGT 367, km 583, 5000, Alto da Jacuba, 39.100-000 Diamantina, MG, Brazil.
[*]E-mail: lsilvamorais@hotmail.com

Mixed oxide-covered mesh electrodes containing Sn, Ru, and Ir with a nominal composition of Sn$_{0.5}$Ir$_x$Ru$_{(0.5-x)}$O$_2$ were prepared by thermal decomposition. The oxide films were supported on stainless-steel fine meshes to generate fluid-permeable electrodes for use in solid polymer electrolyte (SPE) reactors. The surface properties, compositions, and structural properties of the mixed oxides were assessed using scanning electron microscopy (SEM), energy dispersive X-ray spectroscopy (EDS), and X-ray diffraction (XRD) techniques, respectively. The SEM study showed that the mixed oxide coatings had a rough superficial morphology with several cracks and/or fissures. The EDS data revealed a small discrepancy between the nominal and true concentrations of different elements in the ternary mixture, which was attributed to the stock solutions containing precursor salts. From the XRD spectra, it was evident that the mixed oxide thin films display good crystallinity and resulted in formation of a solid solution. Cyclic voltammetry (CV) in acidic solution revealed reversible pseudocapacitive voltammetric behaviour of solid-state surface redox transitions (Ru^{III}/Ru^{IV} and Ir^{III}/Ir^{IV}). In situ surface characterisation of the mixed oxide thin films based on CV and consideration of the intensive dimensionless parameters electrochemical porosity (ϕ) and morphology factor (φ) demonstrated that substituting Ru with Ir in the ternary mixture caused variations in the surface morphology of the electrodes. A linear correlation was verified between the parameters φ and ϕ.

1. INTRODUCTION

Increase in water pollution caused by recalcitrant organic compounds released in the environment demands the development of alternative advanced treatment technologies. A promising alternative to water treatment is available based on the electrochemical advanced oxidation processes

(EAOPs). When appropriate electrode materials are used, the EAOPs enable 'in situ' generation of hydroxyl radicals (HO$^\bullet$ $-$ $E°$ = 2.80 V), which are very effective towards electrochemical combustion/degradation of several types of organic pollutants [1].

In this context, dimensionally stable anodes, based on the preparation of mixed oxide of one or more noble metals and commonly supported on a metallic base such as titanium, are used [2]. Mixed metal oxides (MMOs) with good electrical conductivity may be used in a variety of electrochemical applications of commercial interest; this is because the electrocatalytic properties of these materials may be significantly modulated by changing the composition and/or electrocatalyst preparation conditions [3].

Electrode materials displaying better performance towards the electrochemical combustion of organic pollutants are based on boron-doped diamond (BDD), PbO_2, $Sb-SnO_2$, as well as other kinds of MMOs [4].

Ruthenium oxide (RuO_2) and iridium oxide (IrO_2) have high electrocatalytic activity for the oxygen evolution reaction (OER), which occurs as a side reaction during the combustion of pollutants in aqueous media. Thus, these pure oxides are not very effective towards the electrochemical combustion of organic pollutants. Accordingly, these materials are commonly used in the form of MMOs, in which other elements are added to the oxide mixture to increase the overpotential for OER, thereby improving the electrocatalyst performance for the combustion of organic pollutants.

As reported by Hutchings et al. [5], a $(Sn+Ru+Ir)O_2$ ternary oxide electrocatalyst displayed superior chemical and mechanical stability to the binary $(Ru+Ir)O_2$ electrocatalyst during OER under intense gas evolution. In addition, inclusion of tin oxide (SnO_2) in the $(Ru+Ir)O_2$ binary mixture enables modulation of the electrocatalytic properties of the oxide mixture to increase the OER overpotential, thereby facilitating electrochemical combustion of pollutants. In fact, some researchers [6–8] have reported the use of electrodes consisting of a $(Sn+Ru+Ir)O_2$ ternary mixture for the degradation of organic pollutants.

Nevertheless, there are no literature reports accounting for the use of a $(Sn+Ru+Ir)O_2$ ternary oxide system to fabricate fluid-permeable electrodes (FPEs) for electrochemical degradation of organic pollutants in electrolyte-free water using solid polymer electrolyte (SPE) filter-press reactors. Recently, our research group reported the preparation of mixed oxide−covered mesh electrodes (MOMEs) comprising the $Sb-SnO_2$ and $(Co+Ni)O_y$ systems to fabricate FPEs aimed at the oxidation of organic pollutants [9,10], while the $Fe-PbO_2$ system was applied for the electrochemical ozone production for environmental purposes [11].

The electrocatalytic properties of MMOs depend on factors linked to the film morphology [12], preparation method [13], composition of the electrode [14], and electronic properties [15]. In this respect, several researchers have employed electrochemical techniques (e.g., cyclic voltammetry (CV) and electrochemical impedance spectroscopy (EIS)) for characterising 'in situ' the surface properties of the oxide electrodes. In several cases, the characterisation studies using the CV technique are based on the methodologies proposed by Trasatti et al. [16] and Da Silva et al. [17].

Regarding pure oxides and MMOs systems, the overall electrocatalytic activity for a given electrode reaction may be influenced by the surface areas that are more difficult to access (e.g., 'inner surface') or those easier to access (e.g., 'outer surface') [16–22]. For instance, the chlorine evolution

reaction may be not significantly influenced by the electrode microstructure (inner surface), whereas the OER is affected by presence of surface defects (e.g., deep cracks, narrow pores, etc.) in the oxide's surface structure [2,23].

Studies of the pseudocapacitive voltammetric charge (q^*) as a function of the scan rate of the electrode potential were conducted by Trasatti et al. [16], who defined the 'internal' and 'external' surface areas of oxide electrodes. Afterwards, De Pauli and Trasatti [22] defined the electrode porosity (ϕ) as the ratio between the internal (q_i^*) and total (q_T^*) pseudocapacitive voltammetric charges. In an alternative theoretical treatment, Da Silva et al. [17] proposed a method to determine the differential pseudocapacitances with respect to the internal ($C_{d,i}$) and external ($C_{d,e}$) surface areas of rough/porous electrocatalysts; they also defined the morphology factor (φ) as the ratio between the internal and total pseudocapacitances ($\varphi = C_{d,i}/C_{d,t}$).

The aim of this study is to fabricate and characterise mixed oxide-covered mesh electrodes containing Sn, Ir and Ru, denoted as MOME-$Sn_{0.5}Ir_xRu_{(0.5-x)}O_2$, with $0.1 \le x \le 0.5$, making use of the characterisation methodologies proposed by Trasatti et al. [16,22] and Da Silva et al. [17,18,20].

2. MATERIALS AND METHODS

2.1. Electrode preparation

Mixed oxide-covered mesh electrodes denoted as MOME-$Sn_{0.5}Ir_xRu_{(0.5-x)}O_2$, with $0.1 \le x \le 0.5$ and varying 'x' in steps of 10 mol%, were prepared onto a stainless-steel fine mesh substrate by means of the thermal decomposition of precursor salts ($T = 450$ °C). Five electrodes were prepared in triplicate. Metallic supports (AISI-304: $A_G = 4.0$ cm^2, $\varnothing = 0.125$ mm, and $\varepsilon = 0.075$ mm) supplied by Mesh Co. (Brazil) were previously polished on both sides in water using waterproof emery paper n° 100 to facilitate adherence of the oxide layer on surface of the metallic substrate. These supports were immersed in an ultrasonic bath in order to remove the residues. After that, the supports were degreased with isopropanol for 15 min at 24 °C and then cleaned by immersion in boiling nitric acid (50 v/v% solution) for 5 min. Stock solutions of 0.2 mol dm^{-3} were prepared for the following salts: $SnCl_2 \cdot 2H_2O$ (Sigma Aldrich; MW = 225.65 g mol^{-1}), $RuCl_3 \cdot xH_2O$ (Sigma Aldrich; MW = 207.43 g mol^{-1}) and $IrCl_3 \cdot xH_2O$ (Sigma-Aldrich; MW = 298.58 g mol^{-1}) using isopropanol (Labsynth) as the solvent. Appropriate volumes of stock solutions were mixed to obtain the five precursor solutions to generate the different nominal electrode compositions. In each case, the metallic support was previously immersed in precursor solution and the solvent was evaporated in a muffle oven that was pre-heated to 150 °C. This procedure was repeated several times. The electrodes were then subjected to the final calcination at 450 °C for 1.0 h in order to obtain the desired nominal oxide mass of 2.6 mg cm^{-2}.

2.2. Scanning electron microscopy (SEM) analysis

The surface morphology of the MOME-$Sn_{0.5}Ir_xRu_{(0.5-x)}O_2$ electrodes was analysed using a model TM-3000 scanning electron microscope from Hitachi (Japan).

2.3. Energy dispersive X-ray spectroscopy (EDS) studies

The real composition of the MOME-$Sn_{0.5}Ir_xRu_{(0.5-x)}O_2$ electrodes was determined using energy dispersive X-ray spectroscopy (EDS) using a model TM-3000 scanning electron microscope from Hitachi (Japan) coupled to an EDS analyser from Oxford Instruments (United Kingdom). The ZAF correction method was used in all cases.

2.4. X-Ray diffraction (XRD) analysis

The structure of the MOME-$Sn_{0.5}Ir_xRu_{(0.5-x)}O_2$ electrodes were determined using a model XRD-6000 diffractometer from Shimadzu (Japan) using CuKα radiation (λ = 0.15406 nm − 40 kV, and 30 mA) at a scan rate of 1.0 degree min^{-1} covering the 2θ scale of 20–80°. Crystallographica Search-Match (Version 2.0) software was used to analyse the different samples.

2.5. Electrochemical studies

Cyclic voltammetry studies were conducted for the different oxide electrodes in a 0.5 mol dm^{-3} H_2SO_4 solution using a model PGSTAT-128N potentiostat from AUTOLAB (Netherlands). Voltammetric curves were obtained as a function of the scan rate (v/mV s^{-1}) covering the pseudocapacitive potential interval of −0.4 to 1.1 V/SCE (T = 24 °C). In addition, voltammetric curves were also obtained as a function of the scan rate for the pseudocapacitive interval of 0.2 to 0.3 V/SCE.

Following the methodology proposed by Trasatti et al. [16,22], pseudocapacitive anodic voltammetry charge (q_a*) values were obtained by graphical integration (ΔE = −0.4 to 1.1 V/SCE) using the GPES software from AUTOLAB. The experimental values of the 'total' and 'external' anodic voltammetric charges were calculated using the extrapolation procedure reported in refs. [16,22].

The methodology proposed by Da Silva et al. [17,18,20] was applied using the pseudocapacitive potential interval of 100 mV (ΔE = 0.2 to 0.3 V/SCE) in order to attain the theoretical premises reported in ref. [17]. The experimental values of the 'total' and 'external' differential capacitances were calculated using the voltammetric currents measured at 0.28 V/SCE as a function of the scan rate [17].

3. RESULTS AND DISCUSSION

3.1. SEM analysis

The SEM images of the different oxide layers (magnification: 5000×) are shown in Fig. 1. The surface morphology of the oxide layers was rough and characterised by presence of several cracks/fissures. However, the stainless-steel fine mesh substrate was uniformly covered with the oxide layer, thereby preventing exposure of the substrate to the supporting electrolyte. It is worth mentioning

that it was confirmed that the electrochemical electrode response in the pseudocapacitive potential interval was completely isolated from the response of the metallic substrate, which only underwent active corrosion in the acidic environment under the present experimental conditions.
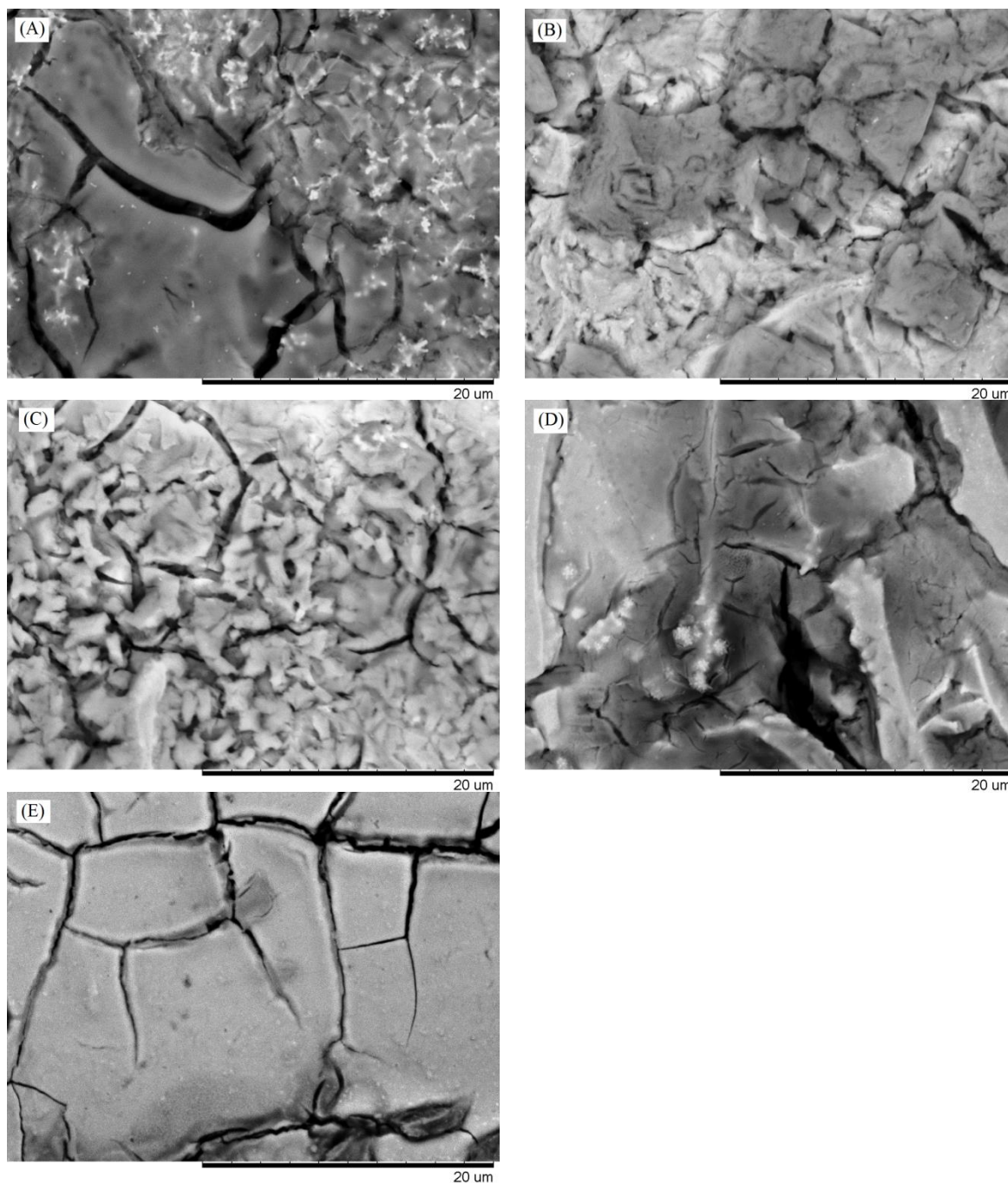
Figure 1. SEM images obtained for the different mixed oxide layers. MOME-$Sn_{0.5}Ir_xRu_{(0.5-x)}O_2$: (A) x = 0.1, (B) x = 0.2, (C) x = 0.3, (D) x = 0.4, and (E) x = 0.5.

3.2. EDS Analysis

The nominal (theoretical) and true compositions (as measured using EDS) of the five MOME-$Sn_{0.5}Ir_xRu_{(0.5-x)}O_2$ electrodes are presented in Table 1. For each sample, the true oxide composition was

obtained for the different surface regions of the oxide mesh structure. In this respect, no significant changes were verified for the true composition as a function of the surface regions where the EDS measurements were carried out. Analysis of Table 1 shows that the true Sn concentration is slightly lower when compared with the nominal one. In addition, small discrepancies between nominal and true compositions were also verified for Ir and Ru. These discrepancies can be attributed to several factors related to electrode preparation, such as preferential volatilization of one or more constituent metal and the use of highly hygroscopic salts to prepare the precursor solutions [13,24,25].

Table 1. Nominal (theoretical) and true (EDS) compositions of the MOME-$Sn_{0.5}Ir_xRu_{(0.5-x)}O_2$ electrodes expressed in terms of atomic percentages (at.%) of the constituent elements.

	Nominal composition			True composition		
Electrode	Mol% Sn	Mol% Ir	Mol% Ru	Mol% Sn	Mol% Ir	Mol% Ru
I	50	10	40	49.0	10.5	40.5
II	50	20	30	48.9	21.5	29.6
III	50	30	20	47.9	32.7	19.4
IV	50	40	10	48.8	39.7	11.5
V	50	50	0	47.7	52.3	0.0

3.3. XRD analysis

Fig. 2 shows X-ray diffractograms of MOME-$Sn_{0.5}Ir_xRu_{(0.5-x)}O_2$. XRD analysis revealed that the mixed oxide thin films display a good degree of crystallinity. According to the Joint Committee on Powder Diffraction Standards (JCPDS) database, the obtained peaks can be attributed to SnO_2 (cassiterite) (PDF# 41-1445 tetragonal structure with $a = b = 4.7382$ Å and $c = 3.1871$ Å and spatial group P42/mnm); IrO_2 (PDF# 15-0870, tetragonal structure with $a = b = 4.4983$ Å and $c = 3.1544$ Å and spatial group P42/mnm); and RuO_2 (PDF# 21-1172, tetragonal structure with $a = b = 4.4902$ Å and $c = 3.1052$ Å and spatial group P42/mnm).

The diffractogram signals designated as 'M' correspond to the metallic support composed of ASTM-304 (PDF# 33-0397, cubic structure with $a = b = c = 3.5911$ Å and spatial group Fm3m). The low relative intensity of the metallic peaks in relation to the mixed oxide peaks confirms that a good mesh coverage with the oxides was obtained, as verified previously in section 3.1 (see SEM study).The metallic oxides that constitute the ternary mixture designated as MOME-$Sn_{0.5}Ir_xRu_{(0.5-x)}O_2$ share the same symmetry group. Moreover, the position of the peaks in Fig. 2 reveals the formation of a solid solution. In agreement with Hume-Rothery's rule, the formation of a solid solution from an oxide mixture depends on the relative differences of the ionic radii of the elements, which cannot exceed 15%. The radii of Sn^{4+}, Ir^{4+}, and Ru^{4+} are 0.060, 0.0625, and 0.062 nm, respectively; this enables the formation of a solid solution [26].

The average size of the oxide crystallites was determined using the Debye-Scherrer equation, taking into account the methodology proposed by Abdullah and Khairurrijal [27], where the (1 0 1)

crystallographic plane was used as the reference. The data obtained in this study are presented in Table 2.

Table 2. Average size of the oxide crystallites with reference to the (1 0 1) crystallographic plane according to the amount of IrO_2 in the MOME-$Sn_{0.5}Ir_xRu_{(0.5-x)}O_2$ electrodes.

Electrode	$t_{(101)}$ / nm
I ($x = 0.1$)	15
II ($x = 0.2$)	13
III ($x = 0.3$)	9
IV ($x = 0.4$)	8
V ($x = 0.5$)	12

Analysis of Table 2 reveals that the oxide crystallites ranged in size from 8 to 15 nm. The smallest values were obtained for oxide compositions containing intermediate IrO_2 values. These data indicate that electrodes with intermediate compositions (e.g., those with $x = 0.3$ and 0.4) may have larger electrochemically active surface areas, as represented by the voltammetric charge and differential capacitance (see section 3.4).
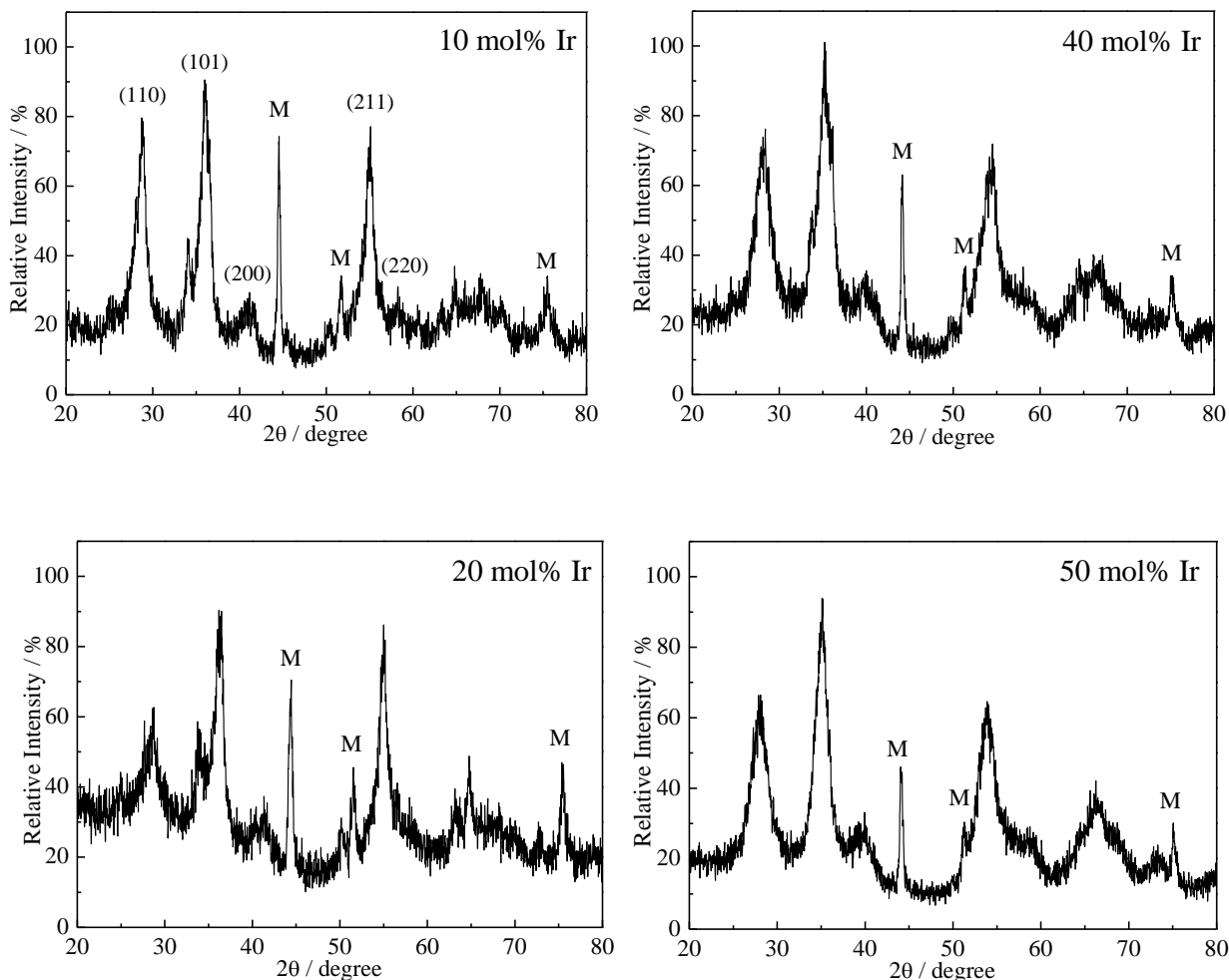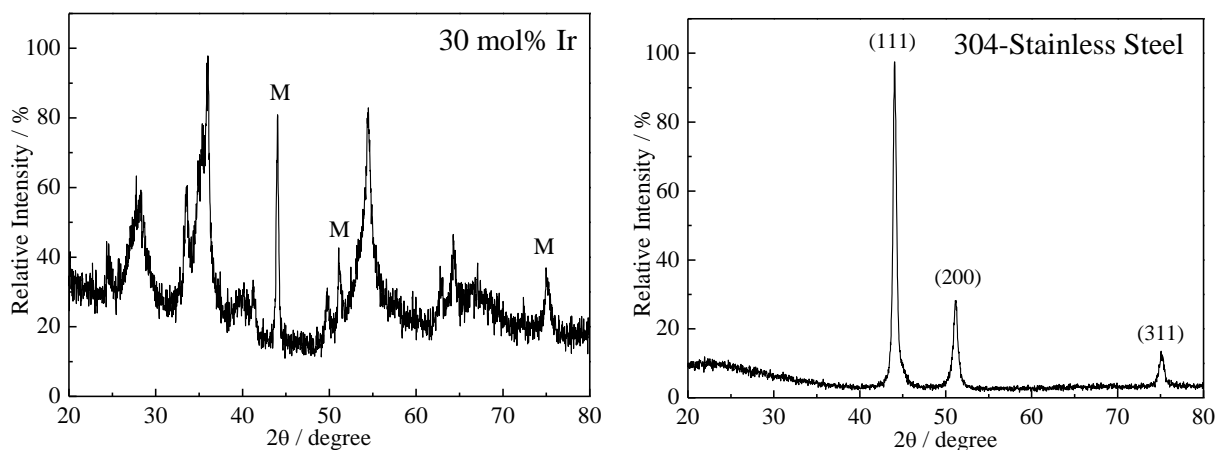
Figure 2. X-Ray diffractograms of the MOME-$Sn_{0.5}Ir_xRu_{(0.5-x)}O_2$ electrodes and stainless-steel metallic substrate.

3.4. In situ surface characterisation of the MOME-$Sn_{0.5}Ir_xRu_{(0.5-x)}O_2$ electrodes

3.4.1. Cyclic voltammetry studies

The surface of the mixed oxide layers were characterised 'in situ' using cyclic voltammetry (CV) with the following conditions: $v = 50$ mV s^{-1}; $\Delta E = -0.4$ to 1.1 V/SCE and 0.5 mol dm^{-3} H$_2$SO$_4$. Fig. 3 shows the voltammetric curves of the different oxide electrodes in the pseudocapacitive potential domain, where solid-state surface redox transitions occur (e.g., Ru(III)/Ru(IV) and Ir(III)/Ir(IV)) in acidic solution [12,20,28,29], which are located between the hydrogen evolution reaction and the OER. The voltammetric curves are only slightly different, showing that substitution of iridium with ruthenium exerts a minor influence on the pseudocapacitive behaviour of the mixed oxide electrodes.
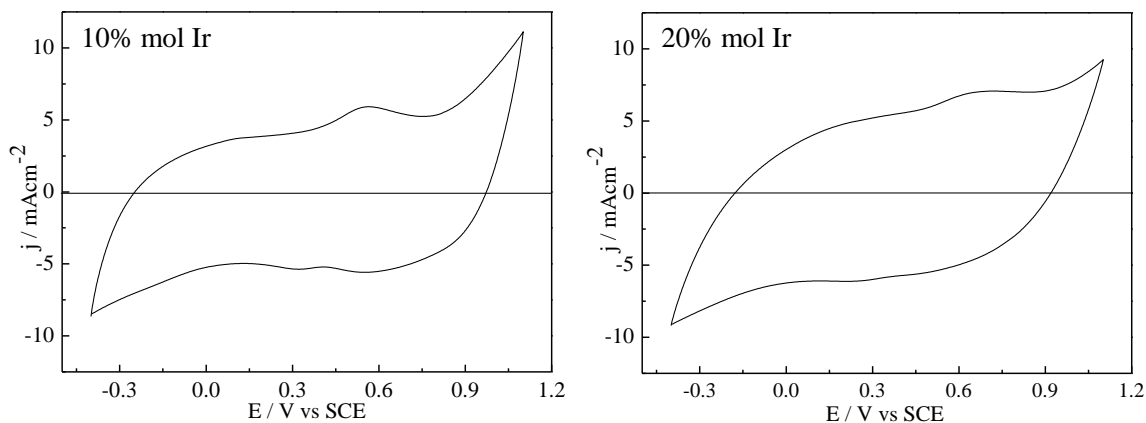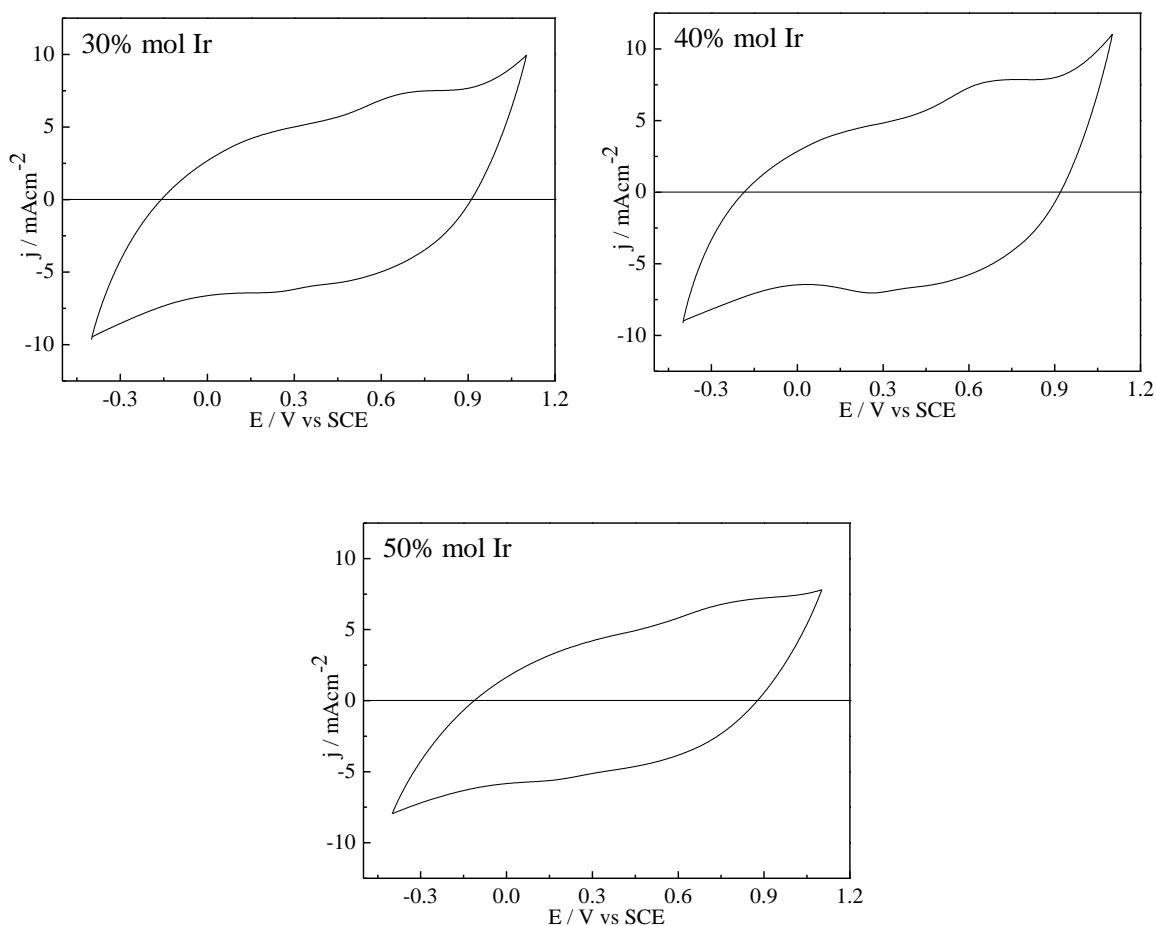
Figure 3. Voltammetric curves of the different oxide electrodes in the pseudocapacitive potential domain. Conditions: MOME-$Sn_{0.5}Ir_xRu_{(0.5-x)}O_2$; 0.5 mol dm^{-3} H_2SO_4; T = 24 °C; and v = 50 mV s^{-1}.

A shift of the anodic peak situated at ~0.56 V (x = 0.1) to a new position located at ~0.76 V (x = 0.5) was verified. These findings are consistent with the different standard values of the redox potentials for the due redox couples (e.g., E^0(Ru(III)/Ru(IV)) = 0.71 V/SCE and E^0(Ir(III)/Ir(IV)) = 0.93 V/SCE).

Fig. 4 shows the values of the apparent anodic (q_a*) and cathodic (q_c*) charge densities with respect to the percentage of IrO_2 in the MOME-$Sn_{0.5}Ir_xRu_{(0.5-x)}O_2$ electrodes.

Fig. 4 shows that the apparent voltammetric charge density for MOMEs increased slightly with increasing amount of IrO_2 reaching a maximum of 72 mC cm^{-2} at 40 mol% IrO_2. It has been reported that ternary mixed oxide electrodes have higher voltammetric charges at intermediate compositions [30–32]. This behaviour may be linked to the formation of smaller crystallites because of differences in the interactions among different kinds of oxides during the sintering process (see data in Table 2), which in turn favours the formation of a more rough oxide surface. In fact, the presence of different metals in mixed oxides can increase the formation of surface defects (e.g., cracks, fissures) when compared to an oxide layer composed by a single oxide [33,34]. It was verified that the ratio of the

anodic and cathodic charge densities is unitary ($q_a^*/q_c^* = 1$), which indicates reversible behaviour of the solid-state surface redox transitions.
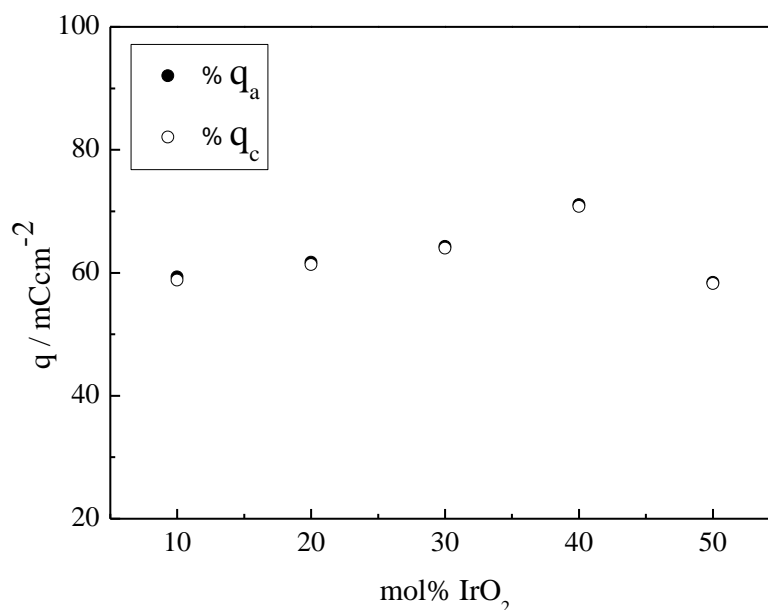
Figure 4. Dependency of apparent anodic (q_a^*) and cathodic (q_c^*) charge densities with respect to the percentage of IrO_2 in the MOME-$Sn_{0.5}Ir_xRu_{(0.5-x)}O_2$ electrodes. Conditions: 0.5 mol dm^{-3} H_2SO_4; $T = 24$ °C; and $\nu = 50$ mV s^{-1}.

3.4.2. Method by Trasatti et al.: inner and outer surface areas for the oxide electrodes

The oxidation states of ruthenium and iridium are dependent on the electrode potential. The solid-state surface redox transitions are coupled to a transfer of hydrated protons at the oxide/solution interface, which is responsible for the pseudocapacitive behaviour (e.g., 'protonic condenser') of the electrodes consisting of conductive oxides. This pseudocapacitive process can be represented by the following equation [16]:

$$MO_x(OH)_y + \delta H^+ + \delta e^- \leftrightharpoons MO_{x-\delta}(OH)_{y+\delta},$$ (1)
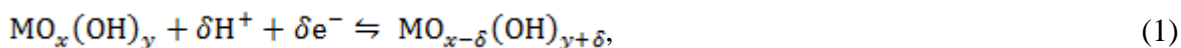
where M (= Ru and/or Ir) is the metal centre of the active surface site, while δH^+ is the amount of protons exchanged with solution.

If each portion of the active surface that is oxidized (or reduced) is considered to be an active surface site for the electrochemical reaction, then the pseudocapacitive voltammetric charge density (e.g., q_a^*) may be viewed as an indirect measurement of the electrochemically active surface area [23,32].

The dependency of the pseudocapacitive voltammetric charge density (q^*) upon the scan rate (ν) can indicate the presence of less accessible regions of the oxide layer to the ionic species present in the electrolyte; these regions are referred to as the 'internal' surface area and includes narrow pores,

deep cracks, etc. These internal surface regions may be progressively excluded from the voltammetric response as the scan rate increases. Trasatti et al. [16] assumed that the total voltammetric charge density (q_t*) is given by two distinct contributions, as follows:

$$q_t^* = q_i^* + q_e^*, \qquad (2)$$

where (q_i*) and (q_e*) are the internal (inner) and external (outer) voltammetric charge densities, respectively.

Considering that the semi-infinite linear diffusion conditions for the transport of protons at the oxide(electrode)/solution interface prevails, Trasatti et al. [16] proposed that the experimentally measured $q*$-values may vary with scan rate (v), $q*(v)$, according to the following equations:

$$q^*(v) = q_e^* + A\left(\frac{1}{\sqrt{v}}\right) \qquad (3)$$

$$\frac{1}{q^*(v)} = \frac{1}{q_t^*} + B \cdot \sqrt{v}, \qquad (4)$$

where A and B are arbitrary constants for a particular oxide layer.

Therefore, a linear plot of q^* versus $1/\sqrt{v}$ can be used to determine the external voltammetric charge density (q_e*) by extrapolating the scan rate to infinity ($v \rightarrow \infty$). Accordingly, plotting $1/q^*$ versus $\sqrt{v}$ and extrapolating the scan rate to zero ($v \rightarrow 0$) yields the total voltammetric charge density (q_t^*). Thus, based on the values of the linear coefficients q_e^* and q_t^* obtained by the aforementioned graphic method, the value of the internal voltammetric charge density (q_i^*) may be calculated using the following relation:

$$q_i^* = q_t^* - q_e^*. \qquad (5)$$

Fig. 5 illustrates the graphical treatment proposed by Trasatti et al. [16,22] with the data obtained for the MOME electrode containing 40 mol% IrO_2. Plots similar to these were obtained for the other electrodes used in this study. The intensive dimensionless parameter denoted 'porosity' or 'electrochemical porosity' (ϕ) was defined as the ratio between the internal and total voltammetric charges [22,35]:

$$\phi = \frac{q_i^*}{q_t^*} \qquad (6)$$
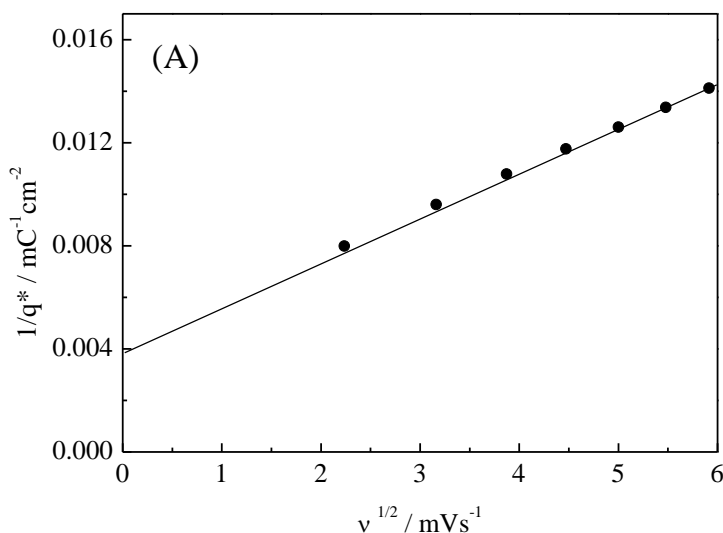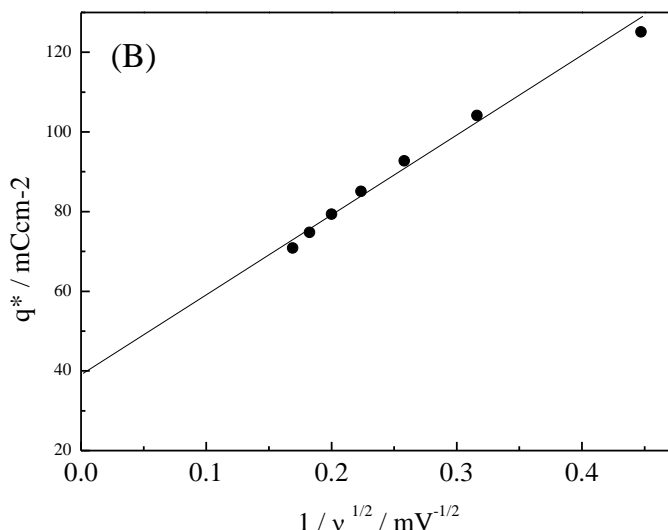
Figure 5. Graphical treatment proposed by Trasatti et al.: (A) $\nu \rightarrow 0$ and (B) $\nu \rightarrow \infty$. Conditions: 40 mol% IrO_2; 0.5 mol dm^{-3} H_2SO_4; $T = 24$ °C.

The greater the value of ϕ the greater the contribution of the inner surface regions of the oxide layer to the total voltammetric charge, that is, high values of ϕ imply that a significant portion of the electrochemically active surface area of the oxide electrode is confined in the deepest regions of the surface defects (e.g., deep cracks, narrow pores, etc.).

Table 3 shows the dependence of the different anodic voltammetric charge densities and electrochemical porosities as a function of the composition of the MOME-$Sn_{0.5}Ir_xRu_{(0.5-x)}O_2$ electrodes. Both the q_t^* and ϕ values strongly depend on the electrode composition. Significant changes are verified for q_i^* while the q_e^*-values remained virtually unchanged. High ϕ-values (e.g., $\phi > 0.5$) were obtained for all oxide electrodes and indicate that the electrochemically active surface area is mainly confined in the inner regions of the oxide coatings.

Table 3. Total (q_t^*), internal (q_i^*) and external (q_e^*) anodic voltammetric charge densities and the electrochemical porosity (ϕ) obtained for the MOME-$Sn_{0.5}Ir_xRu_{(0.5-x)}O_2$ electrodes.

Electrode	q_t^*/mC cm^{-2}	q_e^*/mC cm^{-2}	q_i^*/mC cm^{-2}	ϕ
I ($x = 0.1$)	146	36	110	0.75
II ($x = 0.2$)	235	36	199	0.85
III ($x = 0.3$)	298	34	263	0.88
IV ($x = 0.4$)	372	30	342	0.92
V ($x = 0.5$)	363	26	336	0.93

The voltammetric study applying the methodology proposed by Trasatti et al. [16,22,35] enables unique 'in situ' surface characterisation of the conductive metallic oxide electrodes. In fact, it is virtually impossible for two distinct oxide electrodes to have the same values for the extensive and intensive parameters represented by q_t^* and ϕ, respectively. Therefore, when these two parameters are

analysed together, they constitute a kind of electrochemical identity (e.g., a 'fingerprint') for the oxide electrodes.

3.4.3. Method proposed in this work: the morphology factor of oxide layers

From an electrostatic viewpoint, the total capacitive current density, due to double-layer charging and pseudocapacitive processes, flowing at the electrode(oxide)/solution interface during the linear scan of the electrode potential (E) may be represented by the following equation [17]:

$$j_c = C_d v \left[1 - \exp\left(\frac{-\Delta E}{R C_d v} \right) \right], \tag{7}$$

where j_c is the total capacitive current density, C_d is the total differential capacitance of the electrode/solution interface, R is the sum of all ohmic components of the system (e.g., solution, oxide film, and intra-pore resistances), and $\Delta E = E(t) - E^*$, where E^* is the potential at the start of scan ($t = 0$ and $j_c = 0$).

As demonstrated previously by Da Silva et al. [17], it can be seen from eq. 7 that, for a given v-value, the following linear relation can be obtained when $E(t) \gg E^*$:

$$j_c = C_d v \tag{8}$$

Experimentally, the $E(t) \gg E^*$ condition required for eq. 8 to be applied can be reached by employing j_c-values obtained close to the vertex potential [17]. Therefore, from the experimental variation of $j_c(E)$ with v, the experimental value of C_d can be calculated as follows:

$$C_d = \left(\frac{\partial j_c}{\partial v} \right)_E \tag{9}$$

Normally, the plot of $j_c(E)$ versus v obtained for rough/porous oxide electrodes consists of two linear regions distributed in the low and high domains of scan rate [17−21,36−38]. Thus, in contrast to the behaviour exhibited by a classical parallel-plate capacitor where only a capacitance value is observed, the voltammetric behaviour exhibited by rough/porous oxide electrodes indicates that charging the electrode(oxide)/solution interface during a linear scan of the potential might generate two capacitance values [17]. This may be understood from an electrostatic perspective: Considering a non-flat (irregular) surface morphology for which the surface electric field is not uniform, potential cycling at high frequencies (e.g., high v-values) over a short potential interval (e.g., 100−200 mV) causes gradual exclusion of the electrochemical response of the inner surface regions because of reduced penetration of oscillating disturbance (E) in these regions.

In analogy with the studies by Trasatti et al. [16,22], Da Silva et al. [17] proposed that the total capacitive current density ($j_{c,t}$) for electrodes exhibiting a rough/porous surface morphology is composed by contributions from the 'inner' and 'outer' surface regions, as described by the following equation:

$$j_{c,t} = j_{c,i} + j_{c,e}, \tag{10}$$

where $j_{c,i}$ and $j_{c,e}$ are the voltammetric current densities referring to 'internal' and 'external' surface regions of the oxide electrode, respectively. Consequently, by applying to eq. 10 the definition represented by eq. 9, the following interfacial capacitances can be obtained [17]:

$$C_T = C_I + C_E, \tag{11}$$

where C_T, C_I, and C_E are the total, internal, and external differential capacitances, respectively.

Inspired by the 'electrochemical porosity' concept proposed by Trasatti et al. [22,35], Da Silva et al. [17] defined the 'morphology factor' (φ) as an intensive parameter to describe the contribution of the inner surface regions of the oxide layer to the voltammetric response:

$$\varphi = \frac{C_I}{C_T} \tag{12}$$

Despite the apparent similarities of the methodologies proposed by Trasatti et al. [16,22,35] and Da Silva et al. [17], the first methodology is physically based on the existence of a diffusional process at the electrode(oxide)/solution interface, while the latter methodology is based on purely electrostatic concepts, since the electrode(oxide)/solution interface is theoretically represented by the linear combination of a capacitor and an equivalent resistor [17].

As previously mentioned by Da Silva et al. [18,20,36], the morphology factor is a very important parameter for in situ characterisation of rough/porous oxide electrodes; this is because several values of φ may be associated with the same C_T ($= C_I + C_E$) value due to the different possibilities of distribution of the surface irregularities on oxide coatings. Nevertheless, for a given combination of C_T and φ, it is very unlikely that the same values for these parameters can be obtained for two or more distinct electrodes. Thus, different oxide electrodes can only have the same *electrochemical identity* if the values of C_T and φ are the same.
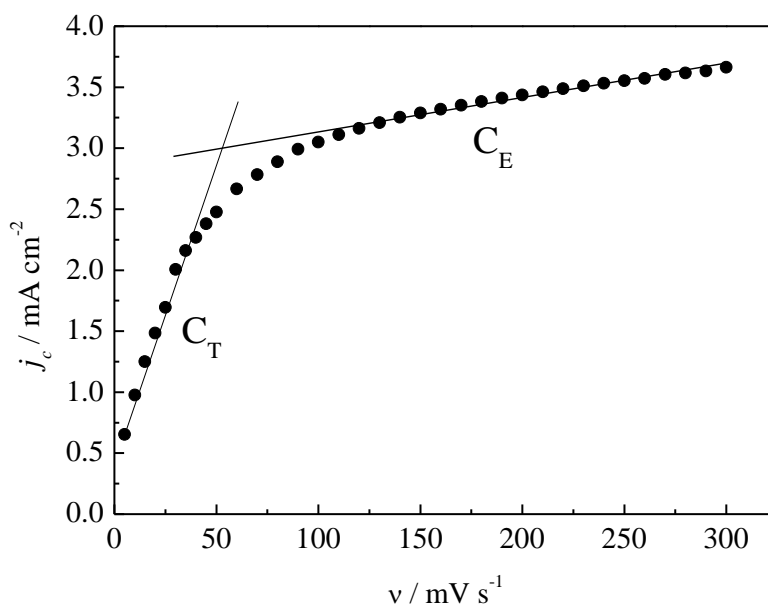
Figure 6. Pseudocapacitive current density (j_c) measured at $E = 0.29$ V/SCE as a function of the scan rate (ν). Conditions: MOME-Sn$_{0.5}$Ir$_x$Ru$_{(0.5-x)}$O$_2$ with $x = 0.1$; $\Delta E = 0.20–0.30$ V/SCE; 0.5 mol dm^{-3} H$_2$SO$_4$; $T = 24$ °C.

As recommended by Da Silva et al. [17], pseudocapacitive voltammograms to determine the total and external differential capacitances can be obtained using a short potential interval (e.g., $\Delta E = 100$ mV) in order to maximize the exclusion of the inner surface regions as the scan rate is increased.

Fig. 6 shows a representative plot of the pseudocapacitive current measured at $E = 0.29$ V/SCE as a function of the scan rate obtained for the MOME-$Sn_{0.5}Ir_xRu_{(0.5-x)}O_2$ electrodes. As can be seen, there are two well-defined linear regions distributed in the low and high domains of the scan rate. This kind of behaviour has already been verified by several authors for different electrode materials [21,37–39].

The total (C_T) and external (C_E) pseudocapacitance values were obtained from the data presented in Fig. 6 according to the slopes obtained in the low and high scan rate domains, respectively. The internal pseudocapacitance (C_I) and morphology factor (φ) values were calculated using eqs. 11 and 12, respectively.
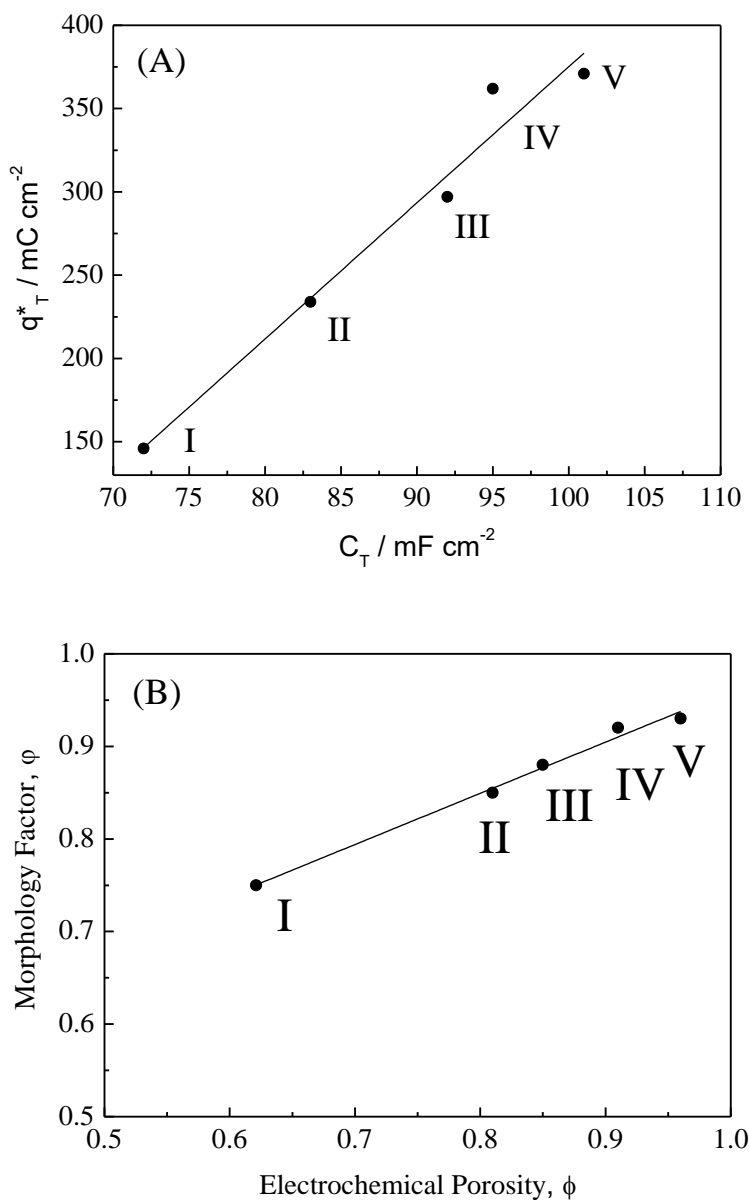
The extensive surface parameters (C_T, C_I, and C_E) and morphology factor (φ) values obtained for the different electrodes are presented in Table 4. As can be seen, an increasing IrO_2 concentration increases the morphology factor, i.e., the substitution of RuO_2 with IrO_2 in the ternary mixture contributes to increasing the surface concentration of active sites in the inner surface regions of the oxide films. Moreover, the IrO_2 concentration has caused changes in C_T, C_I, and C_E values.

The increase in the IrO_2 concentration in the ternary oxide mixture influences the extent of the total electrochemically active surface area represented by C_T, where this parameter was maximised for the electrode containing 40 mol% IrO_2. Furthermore, the data in Table 4 shows that gradual substitution of Ru with Ir in the ternary mixture systematically reduces the C_E values and increases the C_I values. The highest φ-value was obtained for the electrode containing 50 mol% IrO_2. Overall, the high φ-values (e.g., $\varphi > 0.5$) obtained for different MOME-$Sn_{0.5}Ir_xRu_{(0.5-x)}O_2$ electrodes suggest that the majority of the electrochemically active surface area is confined in the inner surface regions of the oxide films.

Table 4. Extensive (C_T, C_E, and C_I) and intensive (φ) surface parameters obtained for the MOME-$Sn_{0.5}Ir_xRu_{(0.5-x)}O_2$ electrodes.

Electrode	C_T/mF cm^{-2}	C_E/mF cm^{-2}	C_I/mF cm^{-2}	φ
I ($x = 0.1$)	72	27	44	0.61
II ($x = 0.2$)	83	16	67	0.81
III ($x = 0.3$)	92	13	78	0.85
IV ($x = 0.4$)	101	8	93	0.92
V ($x = 0.5$)	95	4	92	0.97

Figs. 7A and 7B show the linear correlations between the extensive (C_T and q_t^*) and intensive (φ and ϕ) surface parameters, respectively. According to these findings, there is a good correlation between the different methodologies proposed by Trasatti et al. [16] and by Da Silva et al. [17].

Figure 7. Linear correlation between the extensive (A) (C_T and q_t^*) and intensive (B) (φ and ϕ) surface parameters obtained for the MOME-$Sn_{0.5}Ir_xRu_{(0.5-x)}O_2$ electrodes.

Overall, the data presented in Fig. 7 suggest that both C_T and q_t^* may be used to represent the extension of the electrochemically active surface area. In addition, both φ and ϕ may be used as intensive parameters to characterise the rough/porous surfaces exhibited by oxide electrodes. The analogy between φ and ϕ has also been recently verified by Wu et al. [40] and Rashkova et al. [41].

The use of different methodologies discussed in this study which are based on the cyclic voltammetry technique is very important for heterogeneous electrocatalysis studies. In fact, while q_t^* and C_T provide an indirect measure of the total electrochemically active surface area, ϕ and φ represent the fraction of the total electrode surface area (more difficult-to-access regions) which may contribute less or even be inactivated during intense gas evolution (e.g., OER). Besides, electrodes showing high

φ or φ values are, at least in principle, more prone to mechanical wear caused by local pressure fluctuations during intense gas evolution since they can have a more fragile (less compact) surface structure.

A survey of the literature shows that several authors have used the methodology proposed by Trasatti et al. [16,22,35] to characterise many types of oxide electrodes [34,42–45]. Accordingly, the methodology reported by Da Silva et al. [17] has been used by several authors to characterise different kinds of electrode materials, predominantly based on conductive metallic oxides [19,21,38,39,46–48]. As an exception, Santana et al. [38] employed the latter methodology for the in situ characterisation of rough electrodes consisting of boron-doped diamond.

4. CONCLUSIONS

Ternary mixed oxides containing Sn, Ir, and Ru were supported on a stainless-steel fine mesh substrate using the thermal decomposition method. These electrodes were denoted as MOME-$Sn_{0.5}Ir_xRu_{(0.5-x)}O_2$. SEM studies revealed that the oxide layers exhibit a rough surface morphology containing many cracks/fissures. XRD analysis revealed the formation of a solid solution for ternary oxide mixtures containing different concentrations of IrO_2. Analysis of the voltammetric curves in the pseudocapacitive potential domain revealed the occurrence of solid-state surface redox transitions reactions for the different oxide electrodes.

The in situ surface characterisation study of oxide electrodes employing the methodology proposed by Trasatti et al. revealed that both the total charge (q_t^*) and electrochemical porosity (φ) values are very dependent on the substitution of Ru with Ir in the ternary oxide mixture. In good agreement, the in situ surface characterisation study conducted using the methodology proposed by Da Silva et al. revealed that substituting Ru with Ir in the ternary oxide mixture caused an increase in the extension of surface area represented by the total differential capacitance (C_T). In addition, the intensive surface parameter defined as morphology factor (φ) was strongly affected by the oxide composition.

A good linear correlation exists between the extensive (C_T and q_t^*) and intensive (φ and φ) surface parameters obtained using the different aforementioned methodologies. These results indicate that the extension of the electrochemically active surface area of the oxide electrodes may be represented by both C_T and q_t^*. Also, both intensive parameters φ and φ may be used to characterise the surface morphology of the mixed oxides electrodes.

References

1. Ch. Comninellis, *Electrochim. Acta*, 39 (1994) 1857–1862.

2. S. Trasatti, *Electrochim. Acta*, 45 (2000) 2377–2385.
3. M.E. Makgae, C.C. Theron, W.J. Przybylowicz, A.M. Crouch, *Mater. Chem. Phys.*, 92 (2005) 559–564.
4. Ch. Comninellis, G. Chen (eds.), *Electrochemistry for the Environment*, Springer, New York, 2010.
5. R. Hutchings, K. Müller, R. Kötz, S. Stucki, *J. Mater. Sci.*, 19 (1984) 3987–3994.
6. S. Chellammal, P. Kalaiselvi, P. Ganapathy, G. Subramanian, *Arab. J. Chem.*, 9 (2016) S1690–S1699.
7. M.E. Makgae, M.J. Klink, A.M. Crouch, *Appl. Catal. B Environ.*, 84 (2008) 659–666.
8. C. Regina, C.M.R. Botta, E.L.G. Espindola, P. Olivi, *J. Hazard. Mat.*, 153 (2008) 616–627.
9. L.M. Da Silva, I.C. Gonçalves, J.J.S. Teles, D.V. Franco, *Electrochim. Acta*, 146 (2014) 714–732.
10. F.M. Ribeiro, E.R. Faria, R.M. Verly, D.V. Franco, L.M. Da Silva, *Electrochim. Acta*, 194 (2016) 127–135.
11. L.G. De Sousa, D.V. Franco, L.M. Da Silva, *J. Environ. Chem. Eng.*, 4 (2016) 418–427.
12. L.M. Da Silva, J.F.C. Boodts, L.A. De Faria, *Electrochim. Acta*, 45 (2000) 2719–2727.
13. T.A.F. Lassali, J.F.C. Boodts, L.O.S. Bulhões, *J. Non. Cryst. Solids*, 273 (2000) 129–134.
14. C.P. De Pauli, S. Trasatti, *J. Electroanal Chem.*, 539 (2002) 145–151.
15. S. Ardizzone, S. Trasatti, *Adv. Colloid Interface Sci.*, 64 (1996) 173–251.
16. S. Ardizzone, G. Fregonara, S. Trasatti, *Electrochim. Acta*, 35 (1990) 263–267.
17. L.M. Da Silva, L.A. De Faria, J.F.C. Boodts, *Electrochim. Acta*, 47 (2001) 395–403.
18. É.C.G. Rufino, M.H.P. Santana, L.A. De Faria, L.M. Da Silva, *Chem. Pap.*, 64 (2010) 749–757.
19. G.R.P. Malpass, R.S. Neves, A.J. Motheo, *Electrochim. Acta*, 52 (2006) 936–944.
20. L.M. Da Silva, D.V. Franco, L.A. De Faria, J.F.C. Boodts, *Electrochim. Acta*, 49 (2004) 3977–3988.
21. J.F. Pereira, R.S. Figueiredo, C. Ponce-de-León, R. Bertazzoli, *J. Solid State Electrochem.*, 20 (2016) 1167–1173.
22. C.P. De Pauli, S. Trasatti, *J. Electroanal. Chem.*, 396 (1995) 161–168.
23. S. Trasatti, *Electrochim. Acta*, 29 (1984) 1503–1512.
24. Ch. Comninellis, G.P. Vercesi, *J. Appl. Electrochem.*, 21 (1991) 136–142.
25. É.C.G. Rufino, L.A. De Faria, L.M. Da Silva, *Quim. Nova*, 34 (2011) 200–205.
26. A.T. Marshall, R.G. Haverkamp, *Electrochim. Acta*, 55 (2010) 1978–1984.
27. M. Abdullah, K. Khairurrijal, *J. Nano. Saintek.*, 1 (2008) 28–32.
28. D. Galizzioli, F. Tantardini, S. Trasatti, *J. Appl. Electrochem.*, 4 (1974) 57–67.
29. H. Chen, S. Trasatti, *J. Appl. Electrochem.*, 23 (1993) 559–566.
30. V.A. Alves, L.A. da Silva, J.F.C. Boodts, S. Trasatti, *Electrochim. Acta*, 39 (1994) 1585–1589.
31. T.A.F. Lassali, S.C. de Castro, J.F.C. Boodts, *Electrochim. Acta*, 43 (1998) 2515–2525.
32. S. Trasatti, *Electrochim. Acta*, 36 (1991) 225–241.
33. J. Ribeiro, A.R. de Andrade, *J. Electroanal. Chem.*, 592 (2006) 153–162.
34. J.J. Zhang, J.M. Hu, J.Q. Zhang, C.N. Cao, *Int. J. Hydrogen Energy*, 36 (2011) 5218–5226.
35. G. Spinolo, S. Ardizzone, S. Trasatti, *J. Electroanal. Chem.*, 423 (1997) 49–57.
36. K.C. Fernandes, L.M. Da Silva, J.F.C. Boodts, L.A. De Faria, *Electrochim. Acta*, 51 (2006) 2809–2818.
37. M. Merrill, R. Dougherty, *J. Phys. Chem. C.*, 112 (2008) 3655–3666.
38. M.H.P. Santana, L.A. De Faria, J.F.C. Boodts, *Electrochim. Acta*, 50 (2005) 2017–2027.
39. V. Panić, A. Dekanski, V.B. Mišković-Stanković, S. Milonjić, B. Nikolić, *J. Electroanal. Chem.*, 579 (2005) 67–76.
40. W. Wu, Z.-H. Huang, T.-T. Lim, *Appl. Catal. A Gen.*, 480 (2014) 58–78.
41. V. Rashkova, S. Kitova, T. Vitanov, *Electrochim. Acta*, 52 (2007) 3794–3803.
42. T. Audichon, B. Guenot, S. Baranton, M. Cretin, C. Lamy, C. Coutanceau, *Appl. Catal. B Environ.*, 200 (2017) 493–502.

43. X. Pétrissans, A. Bétard, D. Giaume, P. Barboux, B. Dunn, L. Sicard, J.Y. Piquemal, *Electrochim. Acta*, 66 (2012) 306–312.
44. Y. Chen, L. Hong, H. Xue, W. Han, L. Wang, X. Sun, J. Li, *J. Electroanal. Chem.*, 648 (2010) 119–127.
45. R. Berenguer, C. Quijada, E. Morallón, *Electrochim. Acta*, 54 (2009) 5230–5238.
46. S. Sun, Z.J. Xu, *Electrochim. Acta*, 165 (2015) 56–66.
47. M.H.P. Santana, L.A. De Faria, J.F.C. Boodts, *Electrochim. Acta*, 49 (2004) 1925–1935.
48. S. Palmas, F. Ferrara, A. Vacca, M. Mascia, A.M. Polcaro, *Electrochim. Acta*, 53 (2007) 400–406.